Structure
Article

Rigor to Post-Rigor Transition in Myosin V: Link between the Dynamics and the Supporting Architecture

Riina Tehver[1] and D. Thirumalai[1,2,*]
[1]Biophysics Program, Institute for Physical Science and Technology
[2]Department of Chemistry and Biochemistry
University of Maryland, College Park, MD 20742, USA
*Correspondence: thirum@umd.edu
DOI 10.1016/j.str.2010.01.019

SUMMARY

The detachment kinetics from actin upon ATP binding is a key step in the reaction cycle of myosin V. We show that a network of residues, constituting the allostery wiring diagram (AWD), that trigger the rigor (R) to post-rigor (PR) transition, span key structural elements from the ATP and actin-binding regions. Several of the residues are in the 33 residue helix (H18), P loop, and switch I. Brownian dynamics simulations show that a hierarchy of kinetically controlled local structural changes leads to the opening of the "cleft" region, resulting in the detachment of the motor domain from actin. Movements in switch I and P loop facilitate changes in the rest of the motor domain, in particular the rotation of H18, whose stiffness within the motor domain is crucial in the R → PR transition. The finding that residues in the AWD also drive the kinetics of the R → PR transition shows how the myosin architecture regulates the allosteric movements during the reaction cycle.

INTRODUCTION

The key to understanding the operation of molecular motors lies in deciphering the details of their mechanochemical coupling, i.e., how nucleotide binding, hydrolysis, and release translate into large scale conformational changes and mechanical work. Myosin family belongs to a class of molecular motors in which the chemical energy is efficiently converted to mechanical work. All known myosins, which are ubiquitous in many organisms, use chemical energy in the form of ATP to produce directed movement on actin filaments. Myosins participate in signal transduction, intracellular trafficking, and cell motility (Sellers, 2000). Class V myosins (myoV) are actin-based processive molecular motors whose physiological function is to carry intracellular cargoes such as organelles, membrane vesicles, and mRNA. Mutations in myoV result in neurological defects, albino coat colors in mice, and similar symptoms known as Griscelli syndrome in humans (for review, see Reck-Peterson et al., 2000).

While the functions and kinetic characteristics of myosins vary considerably between classes, the structures of the motor domains within the family share a common architecture (Sellers, 1999; Geeves and Holmes, 1999; Reck-Peterson et al., 2000). The myosin motor domain, which typically has between 700 and 800 residues, is usually divided into subdomains that are linked by common structural elements (loops and switches). The architecture of myoV motor domain (Figure 1A) is generally divided into the N-terminal domain (green), the upper 50 kDa domain (U50; red), the lower 50 kDa domain (L50; blue), and the converter domain (purple). The actin-binding region and the nucleotide-binding region are on the opposite sides of the upper 50 kDa domain (Figure 1A). A prominent cleft that opens and closes depending on the myosin state during the reaction cycle separates the upper and lower 50 kDa domains. The actin-binding region of the lower 50 kDa domain is connected to a converter domain, which is linked to a long lever arm, thus allowing for small changes in the myosin structure and orientation to be amplified. Allosteric transitions from one conformation to another are often described in terms of rigid body movements of the different domains, rotation of the lever arm, and opening and closing of the cleft between upper and lower 50 kDa domains (Sellers, 1999; Houdusse et al., 1999). The key structural elements in the motor domain that control the allosteric communication and play a crucial role in the dynamics of ATP binding-induced detachment of the motor domain from actin are displayed in Figure 1B.

Known for almost a century, a conventional member of the family, myosin II (muscle myosin), has provided a foundation for the description of many molecular motors. Indeed, the functional cycle of myosins, as suggested by Lymn and Taylor (1971), is based on kinetic studies of myosin II and includes several steps involving changing ATPase activity and binding to or disassociating from actin (Figure 1C). The reaction cycle (Figure 1C) shows that in the absence of ATP, the myosin motor domain is in the rigor (R) state, bound to actin. ATP binding causes a conformational change to the post-rigor (PR) state that results in the detachment of myosin from actin (step I in Figure 1C) and possibly a small step forward (Cappello et al., 2007). Subsequently, ATP is hydrolyzed to ADP and Pi, but the products remain bound to the motor (step II in Figure 1C). Binding of the myosin-ADP-Pi complex to actin (step III in Figure 1C) stimulates Pi release, which restores the high affinity of myosin for actin (step IV in Figure 1C) and results in the formation of a strongly

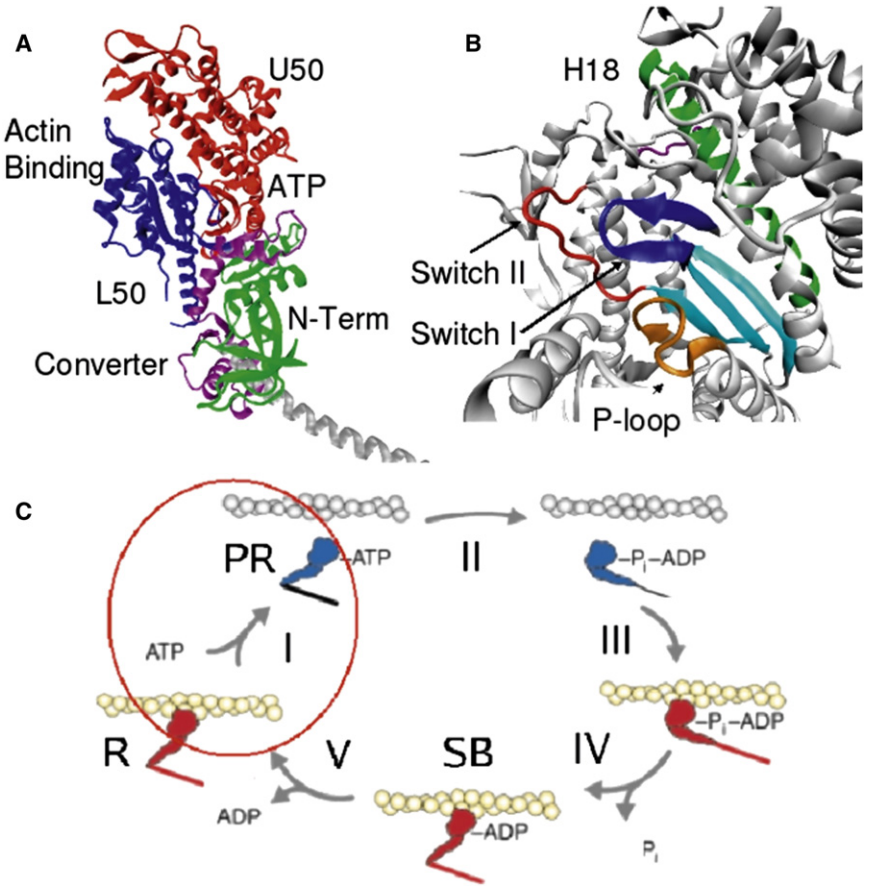

Figure 1. The Subdomains of the MyoV Motor Domain and the Key Structural Elements

(A) The N-terminal domain is shown in green, the upper 50 kDa domain is in red, the lower 50 kDa domain is in blue, and the converter domain is in purple.

(B) To highlight the key structural elements whose movements play a key role in the R → PR transition, we display H18, the central helix in upper 50 kDa domain in green, switch I in dark blue, P loop in orange, switch II in red, the strut in purple, and the central β sheet in light blue.

(C) Schematic diagrams of the reaction cycle showing the predominant states in the Lymn-Taylor cycle of actomyosin [adapted from Murphy et al. (2001)]. Actin-bound states are shown in red and unbound states are in blue. The steps in the cycle are: (I) actin-myosin complex binds ATP and disassociates from actin, (II) ATP is hydrolyzed to Pi-ADP while myosin remains disassociated from actin, (III) subsequent actin binding (IV) accelerates Pi release, and (V) ADP release from myoV completes the cycle. The red circle highlights the (first) step in the cycle, which is the focus of the present study.

bound state (SB in Figure 1C). Finally, the release of ADP completes the cycle (step V in Figure 1C). The power stroke of the two-headed myoV, which results in the stepping of the motor domain along the actin filament, is thought to occur when one of the heads is in the high-affinity SB state. The overall processivity of myosin is critically linked to myoV allosteric transition rates (de la Cruz et al., 1999) and the communication between the two heads. This leads to a precisely coordinated motion, resulting typically in a 72 nm step along the actin track (Vale, 2003; Uemura et al., 2004).

Structural details were added to the reaction cycle (Figure 1C) after the resolution of the class II myosin crystal structure (Rayment et al., 1993b; Fisher et al., 1995). In the rigor actomyosin complex, the 50 kDa cleft is (mostly) closed (Figure 1A). Binding of ATP at the active site causes the cleft to open, disrupting the strong binding interaction between myosin and actin. Hydrolysis of the bound ATP to ADP and Pi results in changes in the 50 kDa cleft that are transmitted via the converter to the lever arm. Following hydrolysis and priming of the lever arm, rebinding to actin could cause further movement of the lower 50 kDa domain relative to the upper 50 kDa domain, which results in release of Pi and subsequently the release of ADP. The release of the nucleotide products results in the closure of the 50 kDa cleft (Fisher et al., 1995) and the rigor actin-myosin complex is restored.

An important aspect of the myosin cycle is the rapid change in myosin affinity for actin upon ATP binding. Precisely timed dissociation of myosin from actin is critical for forward motion. Despite significant progress in the description of the motility of myosin on actin, the structural transitions that occur during the stepping process have not been fully clarified. Here, we study the details of the allosteric communication between different myoV domains that create a connection between ATP binding and myosin disassociation from actin. Because the structures of actomyosin complex are not available, we only consider the R → PR transition of the myoV in isolation. We use normal modes-based structural perturbation method (SPM) (Zheng et al., 2005) to extract a network of residues that are most critical to the R → PR transition. The dynamics of the R → PR transition are probed using Brownian dynamics simulations to follow the time-dependent structural changes within the myoV motor domain in molecular detail. In this paper we answer the following questions pertaining to the R → PR transition: (a) What are the pathways for the communication of the allosteric changes? (b) How are the pathways encoded in the protein structure? (c) What are the underlying hierarchies of structural changes that drive the dynamical changes within the molecule?

We show by applying perturbation at specific locations on the structure of myoV that the communication pathway from the ATP-binding pocket to the actin-binding region involves the P loop, switch I, and helix 18 (H18) using SPM. A network of residues interspersed across the entire motor domain encodes for the pathway. Brownian dynamics simulations show that the global R → PR transition is driven by hierarchy of the movements of key structural elements (Figure 1B) on well separated time scales. Specifically, the binding of ATP triggers fast changes in switch I and the P loop, and their coordinated movement induces

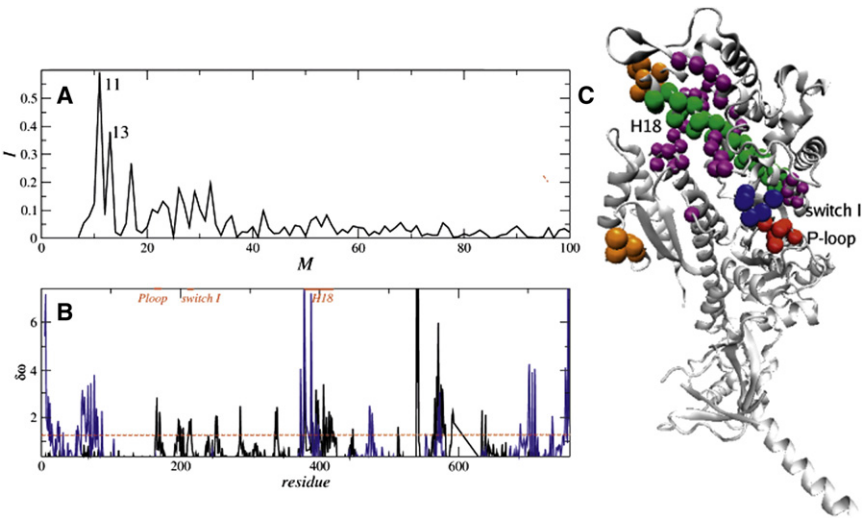

Figure 2. Normal Mode Analysis Using Cα-SC ENM and SPM of MyoV R → PR Transition

(A) The overlap, *I*, of the lowest 100 modes, M, associated with the R → PR transition.

(B) Residue-dependent normalized response to perturbation ($\delta\omega$) for mode 11 in the R → PR transition to imposed strain at a given residue.

(C) The allostery wiring diagram of myoV single motor domain. The Cα atoms of the residues that carry the allosteric signal from the ATP-binding area (blue and red) to the actin-binding area (orange) are shown in purple and green. Helix H18 that is at the center of the path is highlighted in green.

subsequent concerted rearrangements of the rest of the structure, in particular the rotation of H18 and the entire upper 50 kDa domain with respect to the lower 50 kDa domain. It is the relative shift of upper 50 kDa domain, triggered by H18, and lower 50 kDa domain that opens the cleft between the two domains and causes the myosin motor domain to disassociate from actin. The dynamical transitions associated with these structural elements involve coordinated motion of a number of residues identified by the SPM, thus providing a link between kinetics of the R → PR transition and the underlying architecture.

RESULTS AND DISCUSSION

Allostery Wiring Diagram Couples the ATP-Binding Site to the Actin-Binding Region

We used a normal mode analysis-based SPM (Zheng et al., 2005) to determine the network of residues that are energetically most critical to R → PR transition (see Experimental Procedures and Supplemental Experimental Procedures available online for details). Such a network is referred to as the allostery wiring diagram. The normal mode analysis, based on the elastic network model (ENM) of myoV rigor structure (1OE9.pdb) (Coureux et al., 2003) shows that the R → PR (1W7J.pdb) (Coureux et al., 2004) transition is well described by two low frequency modes (Figure 2A). Mode 11, the most significant mode, has an overlap of $I_{11}^{R\rightarrow PR} = 0.6$ (Equation S1 in Supplemental Information), whereas for mode 13, $I_{13}^{R\rightarrow PR} = 0.4$. Mode 11 describes a collective motion of the entire myoV motor domain with the residues of the upper and lower 50 kDa domains moving in opposite directions and accounts for the opening and closing of the cleft between the two domains—a hallmark of the R → PR transition. Mode 13 also describes a collective motion of the entire myoV motor domain, with larger amplitude motions in the N-terminal domain and in the converter.

To determine the residues in the allostery wiring diagram, we calculated the response in mode 11 to a local perturbation (see Figure 2B and Experimental Procedures). The allostery wiring diagram contains residues that ought to break the connection between ATP binding and myosin disassociation from actin. The allostery wiring diagram has 95 residues, including ones in the ATP-binding region (including P loop and switch I), the upper 50 kDa domain residues, the strut (residues Lys569-Glu574), and a set of actin-binding residues (His377-Ala399 and Lys540-Leu543), among others. The locations of all the energetically important residues that drive the R → PR transition are mapped onto the myoV structure (Figure 2C), and a complete list of the residues in the allostery wiring diagram is given in Table S1.

The proposed allostery wiring diagram (Figure 2C) traces a pathway from the ATP-binding site to the actin-binding region and is likely to be responsible for the connection between ATP binding and myoV disassociation from actin. Interestingly, the residues in the allostery wiring diagram span across the key structural elements that drive the kinetics of the R → PR transition. The central structural element that connects the regions is H18 (residues Ser392-His424; see Figure 1B). Given that the long helix H18 has 33 residues, it is striking that the SPM predicts that 30 of those are implicated in the R → PR transition. The importance of H18 in regulating the R → PR transition is further discussed using Brownian dynamics and all-atom simulations (see below).

Mode 13 responds to perturbations somewhat differently. Most of the high $\delta\omega$ (Experimental Procedures) residues in mode 13 belong to the N-terminal domain and the converter. There are seven highly responsive (large $\delta\omega$) residues in H18, whereas in the relay helix six residues have right $\delta\omega$ values. There are no high $\delta\omega$ residues at the ATP-binding site. It is likely that in the R → PR transition these and other less significant modes are dynamically coupled as was shown in the context of allosteric transitions in myosin II (Zheng and Thirumalai, 2009).

Global Kinetics of the R → PR Transition Follow Two-State Kinetics

To link the structural elements identified using the SPM to the dynamics of the ATP-triggered R → PR transition, we performed Brownian dynamics simulations (see Experimental Procedures and Supplemental Experimental Procedures) using the SOP model for the protein (Hyeon et al., 2006a). We started the simulations with the motor in the rigor conformation (1OE9.pdb),

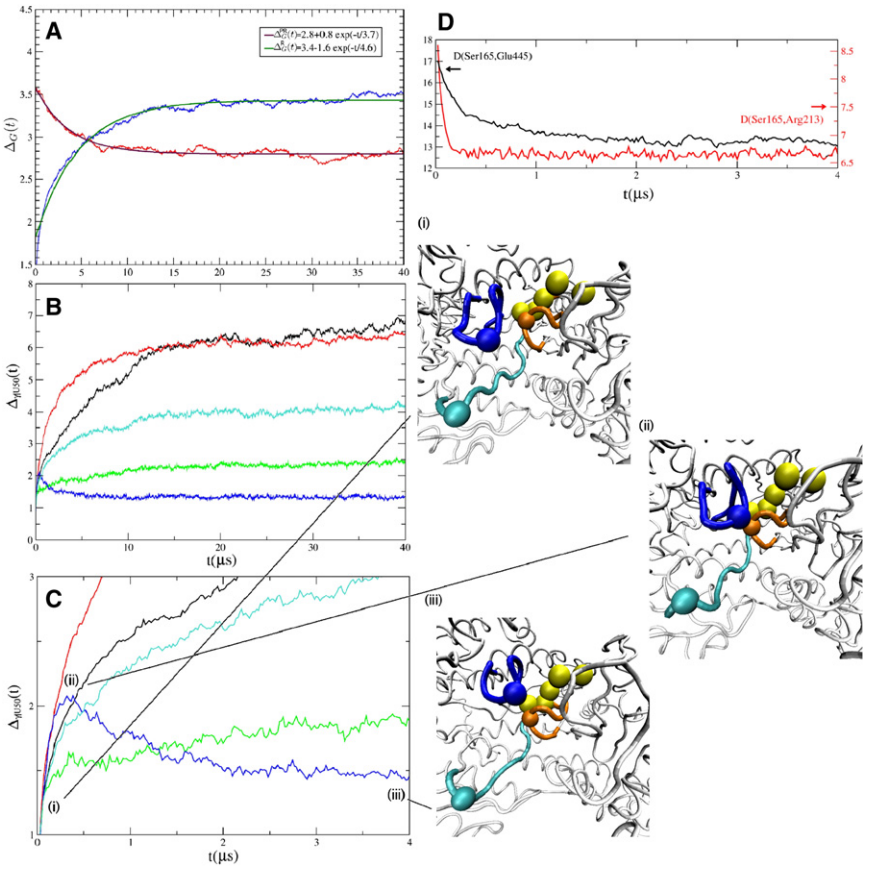

Figure 3. Kinetics of the R → PR Transition

(A) Time-dependent changes in the global rmsd in the R → PR transition, $\Delta_G(t)$, with respect to R (PR) is shown in blue (red). The parameters that describe the fits to the data are in the inset.

(B) Partial rmsd $\Delta_{\lambda|U50}(t)$ (with respect to the rigor conformation) of different structural elements with upper 50 kDa domains aligned. $\Delta_{L50|U50}(t)$ is shown in black, $\Delta_{converter|U50}(t)$ is in red, $\Delta_{strut|U50}(t)$ is in green, $\Delta_{switchI|U50}(t)$ is in blue, and $\Delta_{switchII|U50}(t)$ is cyan.

(C) The first 4 μs of (B) is shown to emphasize the unique role of switch I during the R → PR transition. The "overshot" of switch I past the rmsd value in the PR state is highlighted. (i–iii) The relative positions of the structural elements and residues Ser165 (green), Arg213 (blue), and Glu445 (purple), in three different snapshots, illustrate the three key steps in the dynamics. ATP is shown in red.

(D) The time-dependent distances between switch I residue Arg213 (switch II residue Glu445) and P loop residue Ser165 in red (black).

placed ATP in the binding pocket, and allowed the molecule to equilibrate using a double well potential (Experimental Procedures). Despite variations among individual trajectories (Figure S1), the global transition from R → PR state, which is monitored using root mean square deviation (rmsd) with respect to R and PR states averaged over 100 trajectories, is well fit using single exponentials with characteristic time scales of about 4 μs (Figure 3A). As shown below, the global kinetics masks the complex structural transformations that occur during the allosteric movements from the R to the PR state.

The Subdomains Move in a Concerted Manner

As a first step in analyzing the kinetics of the transition, we probe the structural changes of myoV in terms of rigid body movements of the four subdomains (Houdusse et al., 1999). To the first approximation, allosteric transitions in multisubunit machines in general, and myoV in particular, are usually described as a relative shift in the domains. Indeed, the myoV domains themselves remain rigid throughout the transitions. We have verified this in our simulations by analyzing the structures of individual domains throughout the simulations. In particular, the opening of the cleft, discussed in the Introduction, is a result of the shift of the lower 50 kDa domain and upper 50 kDa domain, which is the fundamental movement that results in the detachment of myoV from actin.

In Figure 3B we plot the changes in the partial rmsds [$\Delta_{\lambda|\gamma}(t)$, where λ and γ are two selected structural elements] of different structural elements. Partial rmsds characterize the structural rearrangements of two subdomains with respect to each other. The characteristic time scale extracted from $\Delta_{\lambda|\gamma}(t)$ describes the movement of λ with respect to γ. To calculate $\Delta_{\lambda|\gamma}(t)$, we align the structural elements γ (e.g., upper 50 kDa domains) of two structures at a time t but calculate the rmsd between the elements λ (e.g., lower 50 kDa domains) only. The time scales obtained from single exponent fits (Figure S2) of the data vary from 3.6 μs for the movement of the converter with respect to upper 50 kDa domain to 7.6 μs for the strut-upper 50 kDa domain movement. The relative motion between the converter and upper 50 kDa domain occurs at 3.6 μs, while the rearrangement between upper 50 kDa domain and switch II takes place in 5.5 μs. The motion between upper 50 kDa domain and lower 50 kDa domain and upper 50 kDa domain and the strut occur in 7.5 μs and 7.6 μs, respectively. Thus, the overall average picture shows a coordinated motion of all subdomains that occur over a range of time scales and cumulatively contribute to the global R → PR transition. Our simulations allow us to provide further details of the structural changes that trigger the global cleft movement.

Synchronous Movements between Switch I and P Loop Drives the Global Motion

The static SPM calculations predict that the residues in the P loop, switch I, the strut, and H18 are critical to the transmission of the allosteric signal from the ATP-binding residues to the actin-binding region. In order to link the static predictions to the transition kinetics, we followed the dynamics of these structural elements more closely. The binding of the nucleotide at the start of our simulations changes many contacts between the P loop and switches I and II. Correspondingly, there are also measurable differences in the $\Delta_{\lambda|\gamma}(t)$s associated with these structural

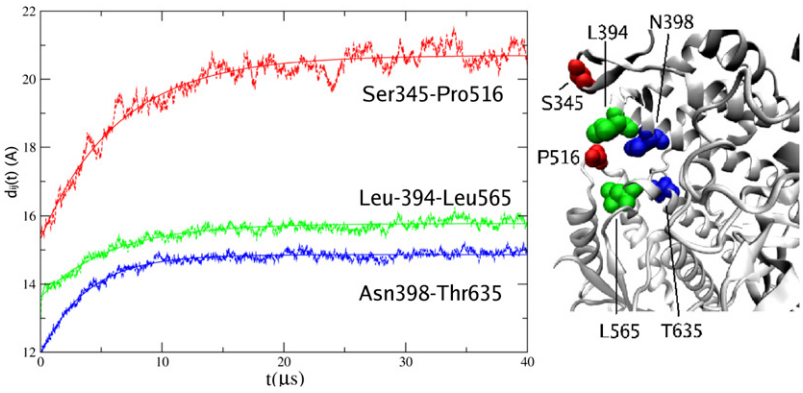

Figure 4. Increase in the Distance d_{ij} between Key Residues *i* and *j* that Describe Cleft Opening

Residues Ser345, Leu394, and Asn398 are located in the upper 50 kDa domain, on one side of the cleft, while residues Pro51 6, Leu565, and The635 are on the opposite side of the cleft. The dashed lines show the data, the solid lines are single exponent fits. The structure on the right shows the residues in the rigor state.

elements when the rigor and post-rigor states are compared. The time-dependent changes in $\Delta_{\lambda|\gamma}(t)$ show (Figures 3B and 3C) that the motion of switch I occurs in two stages. A fast movement toward the P loop (rapid increase in $\Delta_{switchI|U50}(t)$ in Figures 3B and 3C) is followed by a slower relaxation that results in a decrease in $\Delta_{switchI|U50}(t)$. The time scale of the first stage is about 0.1 μs, which is more than an order of magnitude faster than the duration in which other structural changes occur in the R → PR transition. In this phase, switch I makes several new contacts. In particular, Arg213 in switch I makes contacts Ser165 and Gly166 in the P loop during this stage. In the second stage, switch I and P loop move to their post-rigor locations in concert (Figures 3B and 3C), on a characteristic time scale of about 1.7 μs, which is twice as fast as the time scale in which the other significant rearrangements in the myoV motor domain occur (4 μs). Thus, in both stages the dynamical movement associated with switch I and P loop motion precedes most of the other changes that occur in the myoV motor domain.

In Figure 3D, we plot the time-dependent distances between switch I residue Arg213 and P loop residue Ser165 in red and the distances between P loop residue Ser165 and switch II residue Glu445 in black. It is apparent from the plot that P loop and switch I come to contact rapidly while the distance between P loop and switch II changes more gradually. We find that $\Delta_{switchI|U50}$ ($t \approx 0.3$ μs) exceeds the value in the PR state. The overshot may be needed to trigger the rotation of H18. The relative positions of the structural elements at the beginning of the simulation, at about 0.3 μs, and at the end of the simulation are shown in Figure 3 (i–iii).

The time dependence of the motions suggest that the rearrangement of switch I and P loop causes subsequent movements in switch II, shifts in the locations of several residues in the allostery wiring diagram that are located between the loops and H18 (Val250-Glu254 and Val196-Pro201), and the distortion of the β sheet. The subtle changes within the central β sheet (residues Ser158-Ser162, Ser431-Ile438, Gly221-Phe228, and Ile234-Tyr242) were already pointed out elsewhere (Coureux et al., 2004). During the distortion of the β sheet (blue strands in Figure 1B), a few contacts are lost, for example, the contact between residues Tyr242 and Leu647. We have measured the average distance between residues Tyr242 and Leu647 (Figure S3). The characteristic time scale from the exponential fit is 5.1 μs, and thus the distortion of the β sheet happens together with the shifts in the lower 50 kDa, upper 50 kDa, and converter domains.

Kinetic Hierarchy of Local Structural Movements Result in the Opening of the Cleft

One of the most striking structural features that differentiates the rigor state from the post-rigor state is the width of the cleft between upper and lower 50 kDa domains. The closure of the cleft in the rigor state allows residues in both upper 50 kDa domain and lower 50 kDa domain to make contacts with the actin filament. Conversely, the opening of the cleft in the post-rigor state disrupts many of the contacts with actin, thus enabling the disassociation of the motor domain. The importance of the cleft opening is also reflected in the predictions of SPM, which identified a large number of residues in the strut, which is a structural element that bridges the cleft.

We tracked the dynamics of the opening of the cleft using different measures. For instance, the structural rearrangements of the strut [$\Delta_{strut|U50}(t)$], the $\Delta_{L50|U50}(t)$s of the lower 50 kDa domain with the upper 50 kDa domains aligned, or the increase in distances between residues on each side of the cleft all measure the kinetics of the cleft opening. As an example, we show the average separation between residue pairs Leu394-Leu565, Asn398-Thr635, and Ser345-Pro516 as a function of time in Figure 4. The characteristic time scales for the exponential fits are: 3.8 μs for the distance between residues Asn398 and Thr635, 5.8 μs between Leu394 and Leu565, and 6.4 μs for the pair Ser345-Pro516. These values are within a factor of two of the overall transition time. Using the other listed measures [$\Delta_{strut|U50}(t)$, $\Delta_{L50|U50}(t)$], approximately the same time scale emerges.

According to the SPM predictions, a large number of residues in H18 is in the allostery wiring diagram, indicating that this long helix is important to the R → PR transition. The orientation of H18, which is central to the upper 50 kDa domain in the rigor and post-rigor states is shown in Figure 5A. The movement of H18 between the two states can be viewed as a planar rotation (Figure 5A). The Brownian dynamics simulations show that the rotation takes place, on an average, in a two-state manner, with an overall time scale of about 5.8 μs. Interestingly, the end-to-end distance of H18 remains constant during the R → PR transition (see inset in Figure 5B). Thus the opening of the cleft is a result of internal rotation of the helix with an increase of ϕ being about 10°. Cumulatively the R → PR transition is driven by hierarchy of local structural movements with varying time scales. The complexity of local structural transformations are hidden when only $\Delta_G(t)$ (Figure 3A) is considered.

Taken together, the dynamic simulations reveal that a series of well coordinated transformations must occur during the R → PR transition. ATP binding triggers a fast shift of switch I, which makes new contacts with the upper 50 kDa domain and the

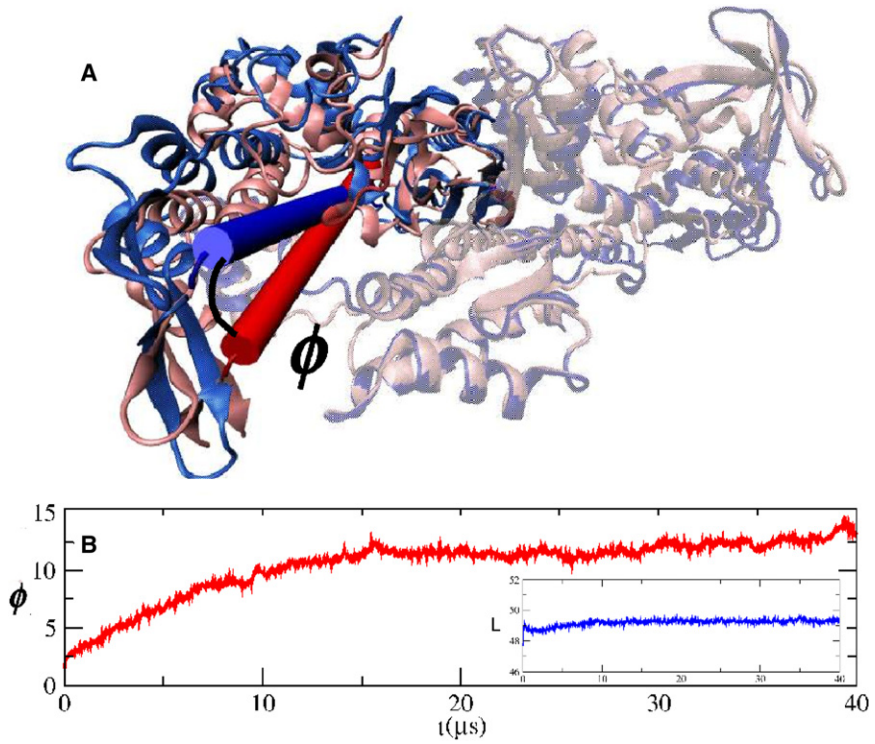

Figure 5. H18 Rotation with Respect to Lower 50 kDa Domain

(A) The angle $\phi(t) = \cos^{-1}[d_{424-392}(t) - d_{424-392}(0)]$, where u(t) is the unit vector associated with $d_{424-392}(t)$, the vector from the Cα atom of residue His424 to the Cα atom of residue Ser392.

(B) Time-dependent changes in ϕ and end-to-end distance L (in Å) (averaged over 100 trajectories) with respect to lower 50 kDa domain.

P loop. In particular, switch I residue Arg213 rapidly makes contact with the P loop central residues Ser165 and Gly1 66. This motion triggers a series of other rearrangements starting with the P loop. Changes in the P loop and the relaxation of switch I to its post-rigor conformation occur on the same time scale. The motions of switch I and P loop trigger changes in the central β sheet and adjacent allostery wiring diagram residues near H18. A rigid body rotation of H18 causes a shift between upper and lower 50 kDa domains, resulting in the opening of the cleft and altering the actin-binding region. As a result of these movements, the affinity of myoV for actin is diminished.

Rigidity of H18 Is Required for the R → PR Transition

The allostery wiring diagram shows that H18 or HO helix (Coureux et al., 2004), which belongs the upper 50 kDa domain and starts near the actin-binding region and extends across the entire domain (Figures 1B and 6A), is particularly significant to the R → PR transition. Structurally, the helix links the ATP and actin-binding sites, and hence must play a central role in the R → PR transition where ATP binding changes the affinity of myosin for actin (Coureux et al., 2004). Figures 6 and Figure S4 display myoV in APO-, ATP-, and ADP-soaked states, highlighting the helix. In all cases, the helix remains highly structured and rigid. H18 with 33 residues and with an end-to-end distance (L) of ~50 Å is also unusually long. The average length of a helix in a globular protein is about ten residues (Branden and Tooze, 1999; Dima and Thirumalai, 2004).

The existence of a long central helix in the upper 50 kDa domain is universal among myosins of different classes and organisms. The persistence of such an unusual structural element indicates that it is likely to play an important role in the motor function. We analyzed the structures of all myosins available in the PDB, and in all cases, there are two long (>30 residues) helices within the motor domain—the relay helix and the

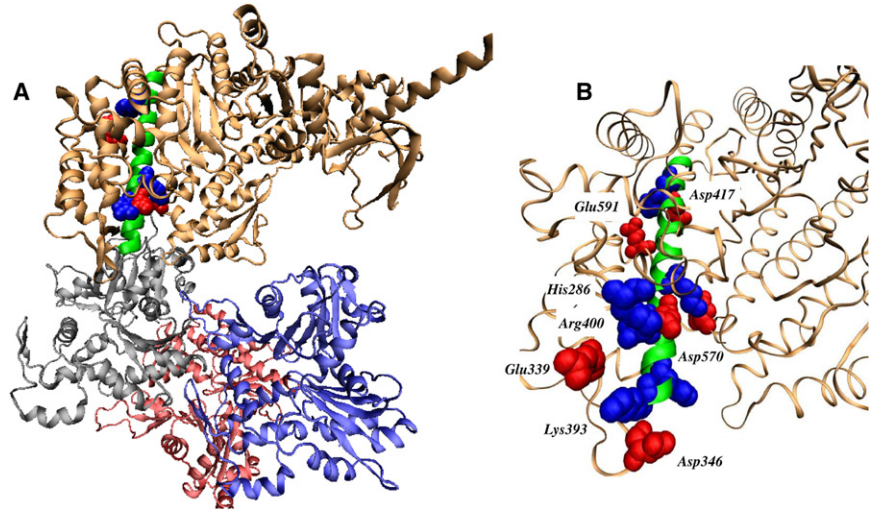

Figure 6. Structural Origin of H18 Rigidity

(A) MyoV (orange) docked to actin (three subunits in gray, red, and blue). H18 is shown in green. H18 and upper 50 kDa domain residues involved in stabilizing electrostatic interactions are shown in van der Waals representation.

(B) Details of interactions that give rise to the stiffness of H18. The salt bridges are formed between the positively charged (blue) and negatively charged (red) residues.

1OE9 392 SKLHAINARDALAKHIYANLFNWIVDHVNKALH
1LXK 341 DCNQAAYSRDALAKALYERLFNWLVSKINTIIN
2BKI 412 KVEQANNARDALAKTVYSHLFDHVVNRVNQCFP
1JX2 421 NVEKSSSSRDALVKALYGRLFLWLVKKINNVLC
2OS8 416 NLQQVINSVGALSKSLYDRMFNWLVKRVNRTLD
1DFK 410 NMNQVVNSVGALAKSLYDRMFNWLVRRVNKTLD
2MYS 418 SEVH__NSVGALAKAVYEKMFLWMVIRINQQLD
2EKW 418 NKDQVTNSIAALAKSLYDRMFNWLVRRVNQTLD

Figure 7. The Pairwise Sequence Alignment of H18 in Different Myosin Structures

The columns list the PDB code, the sequence number for the first aligned residue, the alignment, and the number of positive (+) and negative (−) residues in parentheses. The PDB files used are: 1OE9, chicken myoV; 2OS8, sea scallop myosin II; 1DFK, bay scallop myosin II; 1JX2, dicty myosin II; 2MYS, chicken myosin II; 2EKW, squid myosin II; 1LXK, slime mold myosin I; 2BKI, boar myoVI. Positively charged residues are highlighted in bold and negatively charged residues are in underlined italics.

H18. It has been argued that the relay helix couples the ATPase site and the converter domain, and its rotation is directly linked to the motion of the lever arm during myosin power stoke (Fischer et al., 2005). We propose that the second long helix is analogously used during the myosin allosteric cycle. In this case, it plays a central role in the R → PR transition where it couples the ATPase site and the actin-binding region.

Since the occurrence of H18 with intact structure seems universal among different myosins, we tested its sequence conservation. Surprisingly, the sequence entropy and chemical sequence entropy of the helix within the myosin family (PFAM family PF00063) do not show conservation at sequence level (Figure S5). The pairwise alignment of the myosin sequences, whose structures are available in the PDB (Figure 7), shows the existence of a long helical structure in the upper 50 kDa domain is universal but the sequence varies greatly. In all cases, the helix is predominantly hydrophobic (18 out of 33 residues in myoV) but has a few key charged residues, which play an important role in the stiffness of H18.

The lack of fluctuations in H18 arises due to the formation of both intra-helix salt bridges and those formed with buried charged residues that are spatially adjacent (Figure 6B). The distances between positive-negative charge pairs with one of the charged residues being part of H18 for the myoV structure shows that in all cases the charge-charge pairs remained at the same distance within the accuracy of the crystal structure (~2 Å). Because of their proximity, the interactions between Asp401-Arg400 and Asp570-Lys405 as well as Glu591-His418 should play a particularly significant stabilizing role. In addition to the electrostatic interactions, H18 has a large number of hydrophobic and van der Waals interactions with the upper 50 kDa domain. The total number of contacts between H18 and the upper 50 kDa domain is 93 in the R state and 84 in the PR state. The presence of a large number of contacts not only plays a stabilizing role in reducing the fluctuations in helix end-to-end distance (Figure 5B, inset) but also couples the helix tightly to the domain.

To test the proposal that the rigidity of H18 arises due to intra-peptide salt bridges as well as hydrophobic and electrostatic interactions between neighboring structural elements, we performed all-atom molecular dynamics simulations of the isolated H18. We generated three 10 ns trajectories of H18 in water (see Supplemental Experimental Procedures for simulation details). In all three cases, the helix either significantly shrank in length (by about 15%–20%) or unraveled (Figure S6). We conclude that the interactions between the helix and the rest of the structure must significantly contribute to the rigidity of the helix within the structure. The multiple interactions between the helix and upper 50 kDa domain provide a tight coupling that implies not only that the surrounding environment stabilizes the helix but also that any changes in H18 will be directly transmitted to the surroundings. In short, we can think of H18 as driving the motion of the rest of the upper 50 kDa domain subdomain.

To further illustrate the dynamics of the helix throughout the R → PR transition, we used the 100 trajectories generated using Brownian dynamics simulations. The helix remains rigid and rotates by ~10° with respect to the lower 50 kDa domain (Figure 5A). The end-to-end distance of the helix does not vary significantly, indicating that H18 remains straight throughout the transition (Figure 5B, inset). The angle ϕ (Figure 5B) that characterizes the rotation of the helix with respect to the lower 50 kDa domain, increases smoothly during the transition and changes by ~10°, with a characteristic time scale of ~7 μs (Figure 5B). These results show that we can visualize the R → PR transition as a shift of the upper 50 kDa domain, as carried by the helix, with respect to the lower 50 kDa domain.

SPM Predictions and Mutation Experiments

The allostery wiring diagram (Table S1; Figure 2) delineates a pathway from the ATP-binding site to the actin-binding area. We predict that mutations of switch I, P loop, the strut, and H18 residues would significantly change the R → PR transition in myoV. Many of the predicted residues based on SPM agree with mutation experiments.

Actin-Binding Interface

The myosin actin-binding interface includes residues in both the upper and lower 50 kDa domains on either side of the cleft. Crystal docking studies have identified Tyr626-Gln647, Pro529-His558, Tyr403-Gly416, and Lys567-His578 in chicken skeletal muscle myosin II as part of the actin-binding regions. This list of residues includes Loop 2 (a flexible surface loop of residues Ala624-Lys641) and a surface loop that extends from Arg405 to Lys415 and forms close contacts with residues Pro332 to Glu334 of actin (Rayment et al., 1993a). For chicken myoV, the corresponding actin-binding residues are Asp595-Thr616, Ala501-Leu527, His377-Ile391, and Leu537-Phe548. Even though several of the actin-binding residues (Thr382-Glu385 and Gln594-Glu631) are missing from the crystal structure (1OE9.pdb), we find that out of 95 allostery wiring diagram residues (Table S1), 13 belong to this interface. We identify a large group of residues that are part of the Arg405 to Gly416 loop: His377-Ile391, as well as adjacent residues Leu394-Ala399 and residues Glu539-Leu543 as part of the allostery wiring diagram. The finding that most of the residues that are a part

of or adjacent to Arg405-Gly416 loop is relevant to the R → PR transition is in agreement with previous experimental findings. It has been hypothesized that a mutation of Arg403 leads to a significant change of myosin affinity for actin and related reduction in ATPase activity resulting in decreased power output of cardiac muscle (Sweeney et al., 1994). Mutation of Arg403 to glutamine, leucine, or tryptophan has been linked to hypertrophic cardiomyopathy (for review see Ruppel and Spudich, 1996a). We propose that almost all the residues of this loop are critical to myoV allostery and function. Mutation of *Dictyostelium discoideum* myosin II Glu531 to Gln, or Pro536 to Arg, results in a myosin that is conditionally nonfunctional in vivo (Patterson and Spudich, 1996). In this region, we identify Glu539-Leu543 as allostery wiring diagram residues for the R → PR transition. It is likely that mutations of any of the residues could alter the allostery of myoV.

Knetsch et al. (1999) showed that the deletion of nine residues in Loop 2 affected actin binding and the communication between the actin- and nucleotide-binding sites. Because Loop 2 residues are not resolved in the myoV rigor structure (1OE9.pdb), we carried out SPM analysis of sea scallop myosin II (2OS8.pdb). Several residues in the allostery wiring diagram are located in Loop 2, which further validates our methodology.

P Loop

We identify P loop residues Ser165-Thr170 as well as Val171 as part of the allostery wiring diagram (Table S1). Ruppel and Spudich (1996a) showed that the mutants Gly182Glu and Lys185Arg in *D. discoideum* myosin II (corresponding to Gly166 and Lys169 in chicken myoV) resulted in myosins deficient in ATPase activity and movement in sliding filament assays. They concluded that, because the actin-binding residues of the myosin motor domain had not been altered, the proteins must have remained bound to actin filaments in rigor configuration. Our SPM findings confirm that mutating the P loop residues Ser165-Thr170 would interrupt myoV R → PR transition.

Switch II and Relay Helix

Ruppel and Spudich (1996b) created a bank of random mutations that spanned the *D. discoideum* myosin switch II and relay residues Ile455-His484 (corresponding to residues Gly440-His468 in chicken myoV). They screened the randomly generated mutants for functionality and discovered that the resulting mutated myosins fell into three phenotypic classes (wild-type, intermediate, and null) on the basis of their ability to complement the cytokinesis and developmental defects of the myosin null cell.

Our findings are in agreement with experiments. First, mutations of Ile455, Ser456, Phe461, Lys462, Tyr473, and Phe481 in *D. discoideum* myosin recover wild-type behavior, which agrees with our finding that these residues are not in the allostery wiring diagram. Mutation of Ser465, which is a neighbor of Asn447 that is part of allostery wiring diagram, resulted in an ''intermediate'' myosin. Mutations of other residues such as Thr474, Glu476, His484, Glu459, and Ile460 also resulted in defective myosin functionality. However, the defects could be mainly due to the inability of the myosins to hydrolyze ATP, not their inability to bind the nucleotide (Ruppel and Spudich, 1996b). Our calculations indicate that nucleotide binding and coordinated myosin release from actin should not be inhibited by the mutation of the relay helix (Met467-Gln493) residues.

Other Allostery Wiring Diagram Residues

Nearly 70% of switch I residues (Val196-Asn216) belong to the allostery wiring diagram, which shows that their role is important in the R → PR transition. Switch I, just like P loop or switch II, is a motif common among many ATP-binding proteins. As a result, they play a key role in transitions related to ATP binding, hydrolysis, or release.

Leu565 to Lys581 in the allostery wiring diagram include the strut that runs across the cleft and connects the upper and lower 50 kDa domains (Figure 1A). It is taken for granted that the strut must rearrange in order to accommodate the opening and closing of the cleft that occurs during the myosin cycle. Thus, it is not surprising that mutations of the strut residues could inhibit the required structural changes and thus alter the R → PR transition. A large fraction of allostery wiring diagram residues (30 out of 95) belong to H18 that runs across the upper 50 kDa domain and next to the cleft. To our knowledge, the role of H18 has not been investigated in experiments especially in the context of the R→ PR transition. We predict that H18 plays a key role in the R→ PR transition.

Conclusions

To elucidate the structural changes that take place in the R → PR transition in myoV, which result in the detachment from actin, we used a combination of an ENM and Brownian dynamics using the SOP energy function. The SPM analysis shows that the allostery wiring diagram is made up of a network of residues that connect the ATP- and actin-binding regions. Several of the residues in the allostery wiring diagram have been shown to be important in the allosteric transitions associated with myoV.

Remarkably, the structural elements associated with the allostery wiring diagram are found to be responsible for driving the kinetics of the R → PR transition. The dynamical simulations show that the exponential kinetics associated with the global dynamics mask the hidden complexity of the movements associated with the key structural elements in the R → PR transition. The hierarchy of time scales that drive the global conformational change of the motor domains begins with the movement of switch I toward the P loop (Figure 8). The two structural elements move toward their post-rigor positions on a time scale of about 2 μs, which is a factor of two less than that associated with the decay of $\Delta_G(t)$. The coordinated movement of P loop and switch I triggers a concerted rearrangement of the rest of the structure, in particular the rotation of H18 and the entire upper 50 kDa domain with respect to the lower 50 kDa domain. It is the relative shift of upper 50 kDa domain, carried by H18, and lower 50 kDa domain that opens the cleft between the two domains and causes the myosin motor domain to disassociate from actin.

Although not emphasized here, the broad spectrum of time scales associated with various structural elements also results in the transition state ensemble being plastic (Figure S7). The plasticity of the transition state ensemble in molecular machines in general and myoV in particular may be advantageous in natural adaptation. We would like to note that our calculations were performed with myoV in isolation, without explicitly accounting for interaction with actin. It is likely that the inclusion of actin can dampen internal motions and hence prolong the time scales of the identified local structural changes. As the next step,

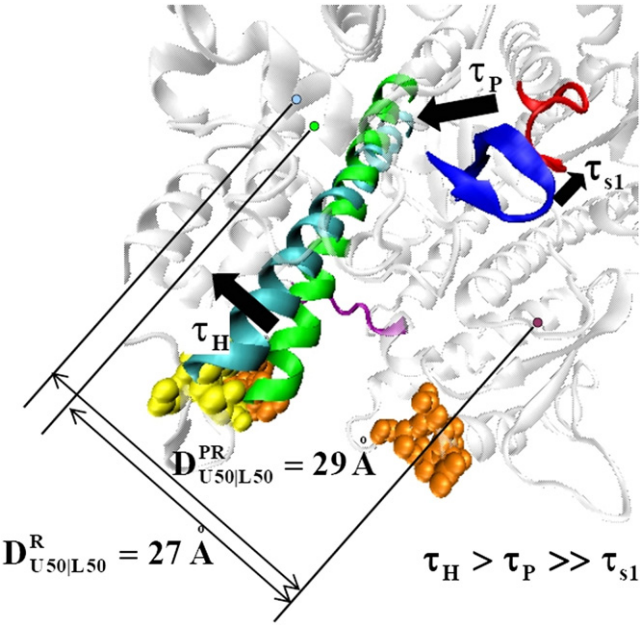

Figure 8. Illustration of the Kinetic Hierarchy of Motions that Drive the R → PR Transition

Upon ATP binding, switch I (blue) rapidly shifts toward the P loop (red) on a time scale of τ_{S1}, which in turn triggers a rotation of H18 (green → cyan) on a time scale τ_P. These internal movements lead to a shift in the upper 50 kDa domain (time scale τ_H), which results in rupture of the contacts between actin and myoV actin-binding residues (orange → yellow). The distance between the centers of mass of the upper 50 kDa domain and lower 50 kDa domain increases during the R → PR transition ($D^R_{U50|L50} < D^{PR}_{U50|L50}$), which facilitates the detachment of myoV from actin.

it will be necessary to explicitly include actin or other cofactors to study their effect on the dynamics of the R → PR transition. Finally, the combination of methods used here should be of general applicability to describe the fundamental steps in the reaction cycle of other molecular motors.

EXPERIMENTAL PROCEDURES

Cα Side Chain Elastic Network Model (Cα-SC ENM)

Applications to a number of systems, especially multimeric protein assemblies, have shown that low frequency modes using the ENM representation with the Cα coordinates alone are sufficient in describing the global motions connecting two allosteric states (Zheng and Doniach, 2003; Bahar and Rader, 2005; Ma, 2005; Sanejouand, 2006). Previously, a variant of ENM, without the benefit of explicit kinetic simulations, has revealed some of the structural movements that occur in the R → PR transition (Cecchini et al., 2008). Recently, we showed that if the ENM is augmented using side chains (Tehver et al., 2009), the important residues at the interface of oligomeric assemblies can also be captured. In Cα-SC ENM, each amino acid (except Gly) is represented using two interaction sites that are centered at the Cα atom and on the centers of mass (R_{SC}s) of the heavy atoms in the side chain. We use the structure of the rigor state of myoV to derive a contact map using the positions of the α-carbon atoms and R_{SC}s. The potential between the sites in contact in the rigor state is taken to be:

$$E = \frac{1}{2}\sum_{i,j:d_{ij}^0<R_c} \kappa_{ij}\left(d_{ij} - d_{ij}^0\right)^2, \quad (1)$$

where d_{ij} is the distance between interaction sites i and j, d_{ij}^0 is the corresponding distance in the native structure, and the constant R_c = 10 Å is the cutoff distance. The site-dependent spring constant matrixA with elements κ_{ij} are calculated using the Betancourt-Thrumalai statistical potential (Betancourt and Thirumalai, 1999) and the van der Waals radii of the side chains (Tehver et al., 2009). The sum is over all pairs of interaction sites that are closer than R_c in the rigor state of myoV. The spectra of normal modes are used to assess global motions connecting the rigor and post-rigor transitions (see Supplemental Experimental Procedures). We chose R_C = 10 Å because the eigenvectors calculated based on this R_C value fitted the experimental B factors in 1OE9.pdb the best. Details of the Cα-SC ENM are given in the Supplemental Experimental Procedures.

Structural Perturbation Method—The Effect of Point Mutations

In order to determine the network of residues that predominantly carry the load during rigor to post-rigor (R → PR) transition, we used the SPM, which probes the response of point mutations (or strain) at site i at all other residues in the structure. Previous studies have shown that the allostery wiring diagram is exquisitely sensitive to the underlying architecture (Tehver et al., 2009). In the context of Cα-SC ENM of myoV, the perturbation at site i is realized by altering κ_{ij} to $\kappa_{ij} + \delta\kappa$. The response $\delta\omega_i$ for mode M is calculated using $\sigma\omega_i = a_M{}^T\, \delta H i\, a_M$, where a_M ($a_M{}^T$) is the eigenvector (transpose of a_M) of mode M and δH is the Hessian corresponding to the perturbation energy (Zheng et al., 2005):

$$\delta E_i = \frac{1}{2}\sum_{j:d_{ij}^0<R_c} \delta\kappa\left(d_{ij} - d_{ij}^0\right)^2. \quad (2)$$

Residues with high $\delta\omega_i$ are likely to be conserved evolutionarily for modes associated with biologically important allosteric transitions. In practice, we selected the residues that had a $<\delta\omega_i>$ larger than twice the average response value to determine the high $\delta\omega_i$ residues.

Self-Organized Polymer Model

To monitor the kinetics of the R → PR transition, we performed Brownian dynamics simulations (Veitshans et al., 1997) using the SOP representation of myoV. In several previous studies of RNA and proteins we have validated the efficiency of the SOP model in a variety of contexts (Hyeon et al., 2006a, 2006b; Chen et al., 2007; Dima and Joshi, 2008). In the SOP model, each amino acid residue is represented by a single interaction site that is centered at the Cα atom. The energy of a conformation, specified by the Cα coordinates r = {r1 . . . rn }, is $H = U_{FENE} + U_N + U_{NN}$, where the various terms are described in the Supplemental Experimental Procedures.

Triggering the Allosteric Transition

The transitions from the rigor (state α) to the post-rigor (state β) conformation were simulated using a double-well SOP potential. The physical rationale for choosing a double-well (or multi-well, in general) potential stems from the realization that different allosteric states correspond to different (local) free energy minima. The energy function for the double-well SOP model with reference conformations α and β is:

$$H = U_{FENE} + U_N^{\beta} + U_N^{\alpha} + U_N^{\alpha\beta} + U_{NN}, \quad (3)$$

where each residue pair is either non-native in both structures (represented by U_{NN}), native in structure α but not β (the potential is given by $U_N{}^{\alpha}$), native in structure β but not α ($U_N{}^{\beta}$), and native in both structures ($U_N{}^{\alpha\beta}$). The non-native potential is given by Equation S2 in Supplemental Information and $U_N{}^{\alpha}$ ($U_N{}^{\beta}$) is the same as in Equation S2 where $r_{ij}^{0\alpha(\beta)}$ refers to native distances in structure α (β). The coupling potential $U_N{}^{\alpha\beta}$ that drives the α ↔ β transition is taken to be:

$$U_N^{\alpha\beta} = \sum_{i=1}^{N-3}\sum_{j=i+3}^{N} \min\left\{\left[\left(\frac{r_{ij}^{0\beta}}{r_{ij}}\right)^{12} - 2\left(\frac{r_{ij}^{0\beta}}{r_{ij}}\right)^{6}\right], \lambda_{\alpha\beta}\left[\left(\frac{r_{ij}^{0\alpha}}{r_{ij}}\right)^{12} - 2\left(\frac{r_{ij}^{0\alpha}}{r_{ij}}\right)^{6}\right]\right\}\varepsilon_h \Delta_{ij}^{\alpha}\Delta_{ij}^{\beta}, \quad (4)$$

where $\Delta_{ij}{}^{\alpha} = 1$ when the distance between two non-covalently bound interaction sites i and j is less than a prescribed cutoff, Rc in a conformation α, and $\Delta_{ij}{}^{\alpha} = 0$ when the distance is greater than Rc. In the simulations, we used Rc = 8 Å (Hyeon et al., 2006a). The factor $\lambda_{\alpha\beta}$, or the ratio of the potential minima between structures α and β, is used to bias the transition toward either

of the structures. In the simulations where we analyzed the $\alpha \rightarrow \beta$ transition, $\lambda_{\alpha\beta} = 0.5$.

Structure Preparation

We used the residues Glu5-Arg792 of chains A of the PDB structures 1OE9.pdb (R) and 1W7J.pdb (PR) for the dynamic simulations. The structures have several missing residues. In order to preserve chain connectivity, we "patched" the missing gaps by inserting the appropriate number of residues into each gap such that the following conditions were met: first, all $C\alpha$-$C\alpha$ distances had to be approximately 3.8 Å, and second, there could not be any steric clashes between the inserted residues and the ones that are structurally resolved. In addition, we considered all non-bonded interactions with the inserted residues to be non-native. The latter condition ensured that non-physical conformations with overlapping residues in the sampling are avoided. Moreover, such a construction did not bias the results toward the allosteric structures. The inserted residues remained mobile.

ATP

Because the R → PR transition is triggered by nucleotide, we used an explicit (coarse-grained) model for ATP. We modeled ATP as five interaction sites, with one at the center of mass of the heavy atoms of the base, one center of mass of the sugar, and the other three phosphate atoms (Figure S8). The energy function for ATP was the same as that for the protein (see Supplemental Experimental Procedures for details). At the start of the simulations, we aligned the nucleotide-binding pockets of the rigor and post-rigor states and the placed the five site ATP into the rigor structure based on its alignment in the post-rigor structure. All interactions between the ATP and myoV were considered repulsive (non-native) in the rigor state. An attractive (native) potential U_N between ATP and myoV was found in the post-rigor state for all the residues that are within the 8 Å cutoff distance to ATP in 1W7J.pdb.

SUPPLEMENTAL INFORMATION

Supplemental Information includes eight figures, three tables, and Supplemental Experimental Procedures and can be found with this article online at doi:10.1016/j.str.2010.01.019.

ACKNOWLEDGMENTS

We thank M. Hinczewski for useful discussions. R.T. is a Ruth A. Kirschstein postdoctoral fellow and her work was supported by the National Institute of General Medical Sciences (1 F32GM082009). D.T. is grateful to the National Science Foundation (CHE 09-14033) and the National Institutes of Health for support.

Received: October 29, 2009
Revised: January 1, 2010
Accepted: January 5, 2010
Published: April 13, 2010

REFERENCES

Bahar, I., and Rader, A.J. (2005). Coarse-grained normal mode analysis in structural biology. Curr. Opin. Struct. Biol. *15*, 586–592.

Betancourt, M.R., and Thirumalai, D. (1999). Pair potentials for protein folding: choice of reference states and sensitivity of predicted motive states to variations in the interaction schemes. Protein Sci. *8*, 361–389.

Branden, C., and Tooze, J. (1999). Introduction to Protein Structure, Second Edition (New York: Garland Science).

Cappello, G., Pierobon, P., Symonds, C., Busoni, L., Christof, J., Gebhardt, M., Rief, M., and Prost, J. (2007). Myosin V stepping mechanism. Proc. Natl. Acad. Sci. USA *104*, 15328–15333.

Cecchini, M., Houdusse, A., and Karplus, M. (2008). Allosteric communication in myosin V: from small conformational changes to large directed movements. PLoS Comput. Biol. *4*, e1000129.

Chen, J., Dima, R.I., and Thirumalai, D. (2007). Allosteric communication in dihydrofolate reductase: signaling network and pathways for closed to occluded transition and back. J. Mol. Biol. *374*, 250–266.

Coureux, P.-D., Wells, A.L., Menetrey, J., Yengo, C.M., Morris, C.A., Sweeney, H.L., and Houdusse, A. (2003). A structural state of the myosin V motor without bound nucleotide. Nature *425*, 419–423.

Coureux, P.-D., Sweeney, H.L., and Houdusse, A. (2004). Three myosin V structures delineate essential features of chemo-mechanical transduction. EMBO J. *23*, 4527–4537.

de la Cruz, E.M., Wells, A.L., Rosenfeld, S.S., Ostap, E.M., and Sweeney, H.L. (1999). The kinetic mechanism of myosin V. Proc. Natl. Acad. Sci. USA *96*, 13726–13731.

Dima, R.I., and Thirumalai, D. (2004). Probing the instabilities in the dynamics of helical fragments from mouse PrPc. Proc. Natl. Acad. Sci. USA *101*, 15335–15340.

Dima, R.I., and Joshi, H. (2008). Probing the origin of tubulin rigidity with molecular simulations. Proc. Natl. Acad. Sci. USA *105*, 15743–15748.

Fischer, S., Windshgel, B., Horak, D., Holmes, K.C., and Smith, J.C. (2005). Structural mechanism of the recovery stroke in the myosin molecular motor. Proc. Natl. Acad. Sci. USA *102*, 6873–6878.

Fisher, A.J., Smith, C.A., Thoden, J., Smith, R., Sutoh, K., Holden, H.M., and Rayment, I. (1995). X- ray structures of the myosin motor domain of *Dictyostelium discoideum* complexed with MgADP.BeFx and MgADP. Biochemistry *34*, 8960–8972.

Geeves, M.A., and Holmes, K.C. (1999). Structural mechanism of muscle contraction. Annu. Rev. Biochem. *68*, 687–728.

Houdusse, A., Szent-Gyorgyi, A.G., and Cohen, C. (1999). Three conformational states of scallop myosin S1. Proc. Natl. Acad. Sci. USA *97*, 11238–11243.

Hyeon, C., Dima, R.I., and Thirumalai, D. (2006a). Pathways and kinetic barriers in mechanical unfolding and refolding of RNA and proteins. Structure *14*, 1633–1645.

Hyeon, C., Lorimer, G.H., and Thirumalai, D. (2006b). Dynamics of allosteric transitions in GroEL. Proc. Natl. Acad. Sci. USA *103*, 18939–18944.

Knetsch, M.L.W., Uyeda, T.Q.P., and Manstein, D.J. (1999). Disturbed communication between actin- and nucleotide-binding sites in a myosin II with truncated 50/20-kDa junction. J. Biol. Chem. *274*, 20133–20138.

Lymn, R.W., and Taylor, E.W. (1971). Mechanism of adenosine triphosphate hydrolysis by actomyosin. Biochemistry *10*, 4617–4624.

Ma, J. (2005). Usefulness and limitations of normal mode analysis in modeling dynamics of biomolecular complexes. Structure *13*, 373–380.

Murphy, C.T., Rock, R.S., and Spudich, J.A. (2001). A myosin II mutation uncouples ATPase activity from motility and shortens step size. Nat. Cell Biol. *3*, 311–315.

Patterson, B., and Spudich, J.A. (1996). Cold-sensitive mutations of Dictyostelium myosin heavy chain highlight functional domains of the myosin motor. Genetics *143*, 801–810.

Rayment, I., Holden, H.M., Whittaker, M., Yohn, C.B., Lorenz, M., Holmes, K.C., and Milligan, R.A. (1993a). Structure of the actin-myosin complex and its implications for muscle contraction. Science *261*, 58–65.

Rayment, I., Rypniewski, W.R., Schmidt-Base, K., Smith, R., Tomchick, D.R., Benning, M.M., Winkelmann, D.A., Wesenberg, G., and Holden, H.M. (1993b). Three-dimensional structure of myosin subfragment-1: a molecular motor. Science *261*, 50–58.

Reck-Peterson, S.L., Provenance, D.W., Jr., Mooseker, M.S., and Mercer, J.A. (2000). Class V myosins. Biochim. Biophys. Acta *1496*, 36–51.

Ruppel, K.M., and Spudich, J.A. (1996a). Structure-function analysis of the motor domain of myosin. Annu. Rev. Cell Dev. Biol. *12*, 543–573.

Ruppel, K.M., and Spudich, J.A. (1996b). Structure-function studies of the myosin motor domain: importance of the 50-kDa cleft. Mol. Biol. Cell *7*, 1123–1136.

Sanejouand, Y.H. (2006). Functional information from slow mode shapes. In Normal Mode Analysis. Theory and Applications to Biological and

Chemical Systems, Q. Cui and I. Bahar, eds. (Boca Raton, FL: Chapman & Hall CRC Press), pp. 91–109.

Sellers, J.R. (1999). Protein Profile: Myosins (Oxford: Oxford University Press).

Sellers, J.R. (2000). Myosins: a diverse *superfamily*. Biochim. Biophys. Acta *1496*, 3–22.

Sweeney, H.L., Straceski, A.J., Leinwand, L.A., Tikunov, B.A., and Faust, L. (1994). Heterologous expression of a cardiomyopathic myosin that is defective in its actin interaction. J. Biol. Chem. *269*, 1603–1605.

Tehver, R., Chen, J., and Thirumalai, D. (2009). Allostery wiring diagrams in the transitions that drive the GroEL reaction cycle. J. Mol. Biol. *387*, 390–406.

Uemura, S., Higuchi, H., Olivares, A.O., De la Cruz, E.M., and Ishiwata, S. (2004). Mechanochemical coupling of two substeps in a single myosin V motor. Nat. Struct. Mol. Biol. *11*, 877–883.

Vale, R.D. (2003). Myosin V motor proteins: marching stepwise towards a mechanim. J. Cell Biol. *163*, 445–450.

Veitshans, T., Klimov, D.K., and Thirumalai, D. (1997). Protein folding kinetics: time scales, pathways, and energy landscapes in terms of sequence-dependent properties. Fold. Des. *2*, 1–22.

Zheng, W., and Doniach, S. (2003). A comparative study of motor-protein motions by using a simple elastic-network model. Proc. Natl. Acad. Sci. USA *100*, 13253–13258.

Zheng, W., and Thirumalai, D. (2009). Coupling between normal modes drives protein conformational dynamics: illustrations Using allosteric transitions in myosin II. Biophys. J. *96*, 2128–2137.

Zheng, W., Brooks, B.R., Doniach, S., and Thirumalai, D. (2005). Network of dynamically important residues in the open/closed transition in polymerases is strongly conserved. Structure *13*, 565–577.